JACS
JOURNAL OF THE AMERICAN CHEMICAL SOCIETY
Article
pubs.acs.org/JACS

Length-Dependent Change of Optical, Magnetic, and Vibrational Properties of Vanadate ($V^{IV}O_3^{2-}$) Quantum Wire Embedded in AM-6 Vanadosilicate

Shuvo Jit Datta and Kyung Byung Yoon*

Korea Center for Artificial Photosynthesis, Center for Nanomaterials, and Department of Chemistry, Sogang University, Seoul 121-742, Korea

Supporting Information

ABSTRACT: AM-6 and VSH-1 are vanadosilicates containing VO_3^{2-} quantum wires and oxovanadate $[O{=}VO_4]^{2-}$ quantum dots, respectively. We developed methods to synthesize pure, highly crystalline, monodisperse, and all-V^{IV} AM-6 and VSH-1 crystals with sizes between 0.2−0.3 and 10 μm. On the basis of their optical, magnetic susceptibility, vibrational, and electron spin resonance (ESR) properties, we have elucidated the following interesting phenomena. The length of the VO_3^{2-} quantum wire (l) linearly increases as the length along the [110] direction $\{L_{[110]}\}$ increases. The band gap energy (E_g) of the VO_3^{2-} quantum wire progressively decreases with increasing l even when it reaches ~210 nm, indicating that the Bohr length (the length at which the quantum confinement effect no longer appears) is longer than 200 nm. The deduced μ_z and μ_{xy} are $0.0005m_e$ and $15.7m_e$, respectively. Per-V^{IV}-ion oscillator strength of the d−d transition increases by 7−9 times and that of CT transition increases by 1.5−1.9 times with increasing l from ~50 to 210 nm (by ~4 times). The longitudinal vibration frequency ν of the VO_3^{2-} quantum wire decreases and the intensity of the vibrational band increases as l increases. The ESR intensity increases while the peak-to-peak width decreases as l increases, indicating that the spin−spin relaxation rate (R_{ssr}) decreases as l increases. The magnetic susceptibility χ decreases as l increases, especially at $T > 125$ K, indicating that the tendency of the d^1 electron spins to orient to the external magnetic field decreases with increasing l.

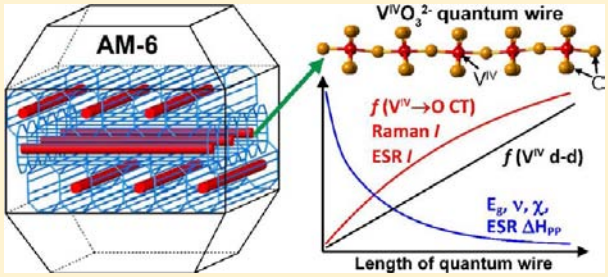

INTRODUCTION

Semiconductor quantum wires with diameters less than a few nanometers have great potential to be used as key materials for nanoscale electronic devices and other novel applications.[1−7] Unlike quantum dots, the length as well as the diameter of the quantum wire sensitively affects its physical properties within the quantum confinement length (defined as Bohr length) region. Therefore, to be able to apply quantum wires for various purposes, information regarding Bohr length and relationships between l and band gap energy (E_g) and between l and oscillator strength for electronic absorption (f), and the longitudinal and transverse reduced masses of exciton (denoted as μ_z and μ_{xy}, respectively) should be elucidated. Furthermore, in such quantum wires, in which unpaired electrons periodically reside on the quantum wires, the relationships between l and electron spin−spin relaxation rate (R_{ssr}), l and magnetic susceptibility (χ), and l and longitudinal vibrational frequencies (ν) should additionally be obtained. However, due to the rarity of semiconductor quantum wires and lack of methods to systematically control l, there is no case whose aforementioned fundamental confinement properties have been thoroughly elucidated.

ETS-10 is a unique titanosilicate that contains regularly spaced TiO_3^{2-} quantum wires with diameter (d) of ~0.67 nm (Figure 1A). They run along the [110] and [1$\bar{1}$0] directions in the crystal, without touching each other.[8−12] Each TiO_3^{2-} quantum wire is surrounded by nanoporous silica with pore size 8 × 5 Å^2 and l usually longer than 50 nm. From the fact that $l \gg d$ and under the assumption that the Bohr length of

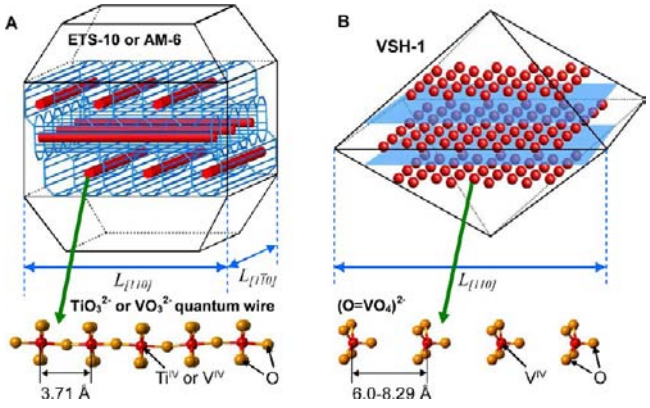

Figure 1. Illustrations of distribution patterns of (A) TiO_3^{2-} or VO_3^{2-} quantum wires in an ETS-10 or AM-6 crystal and (B) $(O{=}VO_4)^{2-}$ quantum dots in VSH-1.

Received: July 23, 2012
Published: September 25, 2012

   dx.doi.org/10.1021/ja307187z | J. Am. Chem. Soc. 2012, 134, 17202−17211

the TiO_3^{2-} quantum wire would be much shorter than 50 nm, Zecchina and co-workers[13] initially proposed that the difference in E_g (ΔE_g) between TiO_3^{2-} quantum wire and bulk titanate should be invariant, based on the mass approximation equation:

$$\Delta E_g = \frac{h^2}{4\mu_{xy}d^2} + \frac{h^2}{8\mu_z l^2} \approx \frac{h^2}{4\mu_{xy}d^2} = \text{constant} \quad (1)$$

where h is the Planck constant and μ_{xy} and μ_z are the transverse and longitudinal effective reduced masses of exciton, respectively.

In contrast, however, our group demonstrated that the Bohr length of TiO_3^{2-} quantum wire is longer than 150 nm and the estimated μ_z value was $0.0006m_e$ (m_e = resting mass of electron),[14] which is much smaller than the smallest reported values (InSb, $0.014m_e$, single-walled carbon nanotube, $0.019m_e$), predicting that the longitudinal exciton mobility is much higher than those of InSb and single-walled carbon nanotube.[15,16] After elucidation of such highly interesting properties of the TiO_3^{2-} quantum wire, it is of great interest to elucidate such important quantum confinement properties from the closely related vanadate ($V^{IV}O_3^{2-}$) quantum wire, which is imbedded in AM-6.[17] In particular, because each V^{IV} ion in the vanadate quantum wire has an unpaired electron residing in a 3d orbital, it is also of great interest to elucidate the relationships between l and the spin-spin relaxation rate (R_{ssr}), l and χ, l and ν, and l and the Raman band intensity of the quantum wire.

AM-6 is isostructural with ETS-10, with $V^{IV}O_3^{2-}$ quantum wires replacing TiO_3^{2-} quantum wires.[17] To elucidate the aforementioned important properties, AM-6 crystals should be synthesized by satisfying the following five basic requirements. First, the crystals should be produced without impurities. Second, the crystallinity should be very high to contain well-preserved VO_3^{2-} quantum wires. Third, the formal oxidation state of all V ions in VO_3^{2-} quantum wires should be +4, without contamination with +5. Fourth, the AM-6 crystals should be uniform in size, or more specifically, the AM-6 crystals should be uniform in l along the [110] direction ($L_{[110]}$) (or along the crystallographically identical $[1\bar{1}0]$ direction, $L_{[1\bar{1}0]}$) along which the VO_3^{2-} quantum wires run. Fifth, the crystals should be produced in different sizes (in different $L_{[110]}$) while the size monodispersity is maintained.

AM-6 was first synthesized by Rocha, Anderson, and co-workers.[17] However, the AM-6 crystals synthesized by them [denoted as AM-6-RA] always contain ETS-10 seed crystals in the center. In this respect, AM-6-RA should better be viewed as an ETS-10/AM-6 core/shell composite material. Furthermore, the synthetic procedure of AM-6-RA always coproduces substantial amounts of quartz as an impurity. Lobo, Doren, and co-workers[18−20] revealed that the VO_3^{2-} quantum wires in AM-6-RA contain both V^{IV} and V^{V}. Sacco and co-workers[21] later reported a method to synthesize ETS-10-free AM-6. However, this AM-6 [denoted as AM-6-S] also contains both V^{IV} and V^{V}. Thus, AM-6-RA and AM-6-S are not suitable to elucidate the aforementioned important properties of the $V^{IV}O_3^{2-}$quantum wire. Furthermore, the crystals of AM-6-RA and AM-6-S have not been produced in uniform sizes.

Recently, we succeeded in synthesizing pure and highly crystalline all-V^{IV} AM-6 crystals having well-preserved VO_3^{2-} quantum wires.[22] However, the developments of the methods to synthesize them in uniform sizes ($L_{[110]}$) and the methods to control their sizes ($L_{[110]}$) have been two additional challenges. We now report the successful development of size-controlled syntheses of pure, highly crystalline, monodisperse, and all-V^{IV} AM-6 crystals with $L_{[110]}$ values of 0.2, 1, 3, 5, and 10 μm and the important confinement properties of the $V^{IV}O_3^{2-}$ quantum wire (Bohr length, μ_{xy}, μ_z, and l-dependent changes of f, ν, R_{ssr}, and χ). We also report the successful size-controlled synthesis of monodisperse VSH-1 crystals,[23] with sizes similar to those of AM-6 crystals, namely, with $L_{[110]}$ = 0.3, 1, 3, 5, and 10 μm (Figure 1B).

VSH-1 is a microporous vanadosilicate material first synthesized by Jacobson and co-workers.[24] It is constructed by interconnecting two-dimensional silicate sheets with square planar oxovanadate $(O{=}V^{IV}O_4)^{2-}$ units (Figure 1B). The reason we simultaneously developed a method for size-controlled synthesis of monodisperse VSH-1 crystals with sizes similar to those of AM-6 crystals was to use the monodisperse VSH-1 crystals as reference materials having isolated V^{IV} centers as a means to demonstrate that the l-dependent changes of f, ν, R_{ssr}, and χ observed from the VO_3^{2-} quantum wire do not arise from the increase in degree of light scattering caused by the increase in crystal size but arise from the increase in l of the quantum wire (vide infra). VSH-1 crystals can also be viewed as crystals bearing isolated V^{IV} quantum dots.

EXPERIMENTAL SECTION

Materials. Sodium silicate (Na_2SiO_3, 35−38% SiO_2, 17−19% Na_2O, Kanto), silica sol (40% aqueous colloidal silica, Ludox HS-40, Aldrich), vanadium oxide (V_2O_5, 99%, Aldrich), vanadium oxide (V_2O_4, 99.9%, Aldrich), sulfuric acid (H_2SO_4, 95%, Duksan), potassium hydroxide (KOH, 95%, Samchun), sodium carbonate hydrated (Na_2CO_3, 99.99%, Aldrich), potassium fluoride (KF, 95%, Samchun), ethanol (EtOH, 95%, SK), and sodium chloride (99.5%, Samchun) were purchased and used without further purification.

Synthesis of A-0.2, A-1, and A-3. Gels consisting of Na_2SiO_3, V_2O_5, H_2SO_4, KOH, EtOH, and distilled deionized water (DDW) were prepared, where the molar ratios of the components SiO_2:V_2O_5:(H_2SO_4):Na_2O:K_2O:EtOH:H_2O were 6.07:1.00:(n):3.03:3.09:7.22:415, where (n) = 3.37, 3.61, and 3.74. The gels were prepared as follows.

Preparation of Si Source Solution. A KOH solution (4.4 g of KOH and 40 g of DDW) was added into the sodium silicate solution composed of 12.2 g of Na_2SiO_3 and 40 g of DDW.

Preparation of V Source Solutions. A required amount of H_2SO_4 (4.2 g for A-0.2, 4.5 g for A-1, and 4.65 g for A-3) was added into a 25-mL round-bottom flask containing DDW (10 g). Subsequently, V_2O_5 (2.2 g) and EtOH (4 g) were sequentially added into the flask. The heterogeneous mixture was refluxed for 45 min, during which the yellow V_2O_5 powder dissolved completely into the solution, and the solution turned greenish-blue. The greenish-blue V source solution was then cooled to room temperature.

The greenish-blue V source solution was added into the Si source solution in a dropwise manner. After the mixture was aged for 15 h at room temperature, the gel was transferred into a 50 mL Teflon-lined autoclave and placed in a preheated oven at 220 °C for 30 h, under a static condition. The precipitated pale yellow crystals were collected, washed, and dried at 100 °C for 1 h, and their X-ray powder diffraction patterns were obtained.

Synthesis of A-5 and A-10. Gels consisting of Na_2SiO_3, V_2O_5, H_2SO_4, KOH, EtOH, and DDW were prepared, where the molar ratios of the components SiO_2:V_2O_5:(H_2SO_4):Na_2O:K_2O:EtOH:H_2O were 5.57:1.00:(n):3.03:3.09:7.22:415, where (n) = 3.31 and 3.46. The gels were prepared as follows.

Preparation of the Si Source Solution. A KOH solution (4.4 g of KOH and 40 g of DDW) was added into the sodium silicate solution composed of 12.2 g of Na_2SiO_3 and 40 g of DDW.

dx.doi.org/10.1021/ja307187z | J. Am. Chem. Soc. 2012, 134, 17202−17211

Preparation of V Source Solutions. A required amount of H_2SO_4 (4.5 g for A-5 and 4.7 g for A-10) was added into a 25-mL round-bottom flask containing DDW (10 g). Subsequently, V_2O_5 (2.4 g) and EtOH (4 g) were sequentially added into the round-bottom flask. The heterogeneous mixture was refluxed for 50 min, during which the yellow V_2O_5 powder dissolved completely into the solution, and the solution turned greenish-blue. The greenish-blue V source solution was then cooled to room temperature.

The cooled greenish-blue V source solution was added into the sodium silicate solution in a dropwise manner. After the mixture was aged for 15 h at room temperature, the gel was transferred into a 50 mL Teflon-lined autoclave and placed in a preheated oven at 225 °C for 36 h, under a static condition. The precipitated pale yellow crystals were collected, washed, and dried, and their X-ray powder diffraction patterns were obtained.

Size-Controlled Synthesis of Monodisperse VSH-1 Crystals (H-*n*). Gels consisting of Ludox (HS-40), V_2O_5, H_2SO_4, KOH, EtOH, and DDW were prepared, where the molar ratios of the components SiO_2:V_2O_5:H_2SO_4:(K_2O):EtOH:H_2O were 4.96:1.00:3.50:(*n*):14.7:233, where (*n*) = 4.87, 5.26, 5.73, 6.13, and 6.47. The gels were prepared as follows.

Preparation of Si Source Solutions. A KOH solution (8.5, 9.2, 10, 10.7, and 11.3 g for H-0.3, H-1, H-3, H-5, and H-10, respectively, and 42 g of DDW) was added into a Ludox HS-40 solution (11 g), and the mixture was stirred vigorously.

Preparation of the V Source Solution. V_2O_5 (2.7 g) and EtOH (10 g) were sequentially added into the 50-mL round-bottom flask charged with a diluted sulfuric acid (H_2SO_4 5.35 g and DDW 20 g). The heterogeneous mixture was refluxed until the solution turned ink blue. The V source solution was cooled to room temperature.

The V source solution was added into the Si source solution in a dropwise manner. After the mixture was aged for 12 h at room temperature, the gel was transferred into a 50-mL Teflon-lined autoclave and placed in a preheated oven at 210 °C for 20 h, under a static condition. The precipitated crystals were collected, washed, and dried at 100 °C for 1 h, and their X-ray powder diffraction patterns were obtained.

Synthesis of Na_2VO_3. A "ceramic method" was employed to prepare polycrystalline Na_2VO_3. Na_2CO_3 and VO_2 were used as starting materials. First, Na_2O was prepared by heating Na_2CO_3 in air for 20 h at 1000 °C, and its weight was measured while it was hot. The 1:1 mixture of Na_2O and VO_2 was ground with a mortar and pestle and then heated at 1150 °C with flowing argon (~50 mL/min) for 12 h. The solid product was collected and ground again and heated again. This cycle of heating and grinding was repeated three times. The XRD patterns of synthesized Na_2VO_3 and theoretical $CaVO_3$ are shown in the Supporting Information.

Preparation of Na^+-Exchanged A-*n* and H-*n* Crystals. The ion exchange was conducted at room temperature for 150 min and repeated five times. First, 1 g of pristine A-*n* or H-*n* powder was introduced into a flask containing 45 mL of 1 M NaCl solution, and subsequently the heterogeneous mixture was mechanically stirred. The ion exchange proceeded up to 90%. Their chemical compositions were determined by inductively coupled plasma atomic emission spectroscopy (ICP-AES) and X-ray fluorescence. Their compositions are (A-*n*) $Na_{1.8}K_{0.2}VSi_5O_{13}{\cdot}xH_2O$ and (H-*n*) $Na_{1.8}K_{0.2}VSi_4O_{11}{\cdot}xH_2O$.

Dehydration of A-*n* and H-*n*. The Na^+-exchanged A-*n* and H-*n* powders were vacuum-dried at 160 and 200 °C, respectively, for 6 h. The dehydrated A-*n* and H-*n* powders were transferred into a glovebox charged with high-purity Ar. Each dehydrated sample (1 g) was transferred into a flat cylindrical quartz cell (i.d. = 19 mm) for UV–vis–NIR and Raman spectral measurements.

Instrumentation. Scanning electron microscopy (SEM) images were obtained on a field-emission scanning electron microscope (JEOL JEM 7600 and Hitachi S-4300) operating at an acceleration voltage of 15 kV. Elemental analyses of various Na^+-A-*n* and Na^+-H-*n* samples for M^{n+}, Si, and V were carried out by ICP-AES and X-ray fluorescence (XRF) analysis. Transmission electron microscopy (TEM) images were collected on a JEOL JEM 4010 microscope. Raman spectra of the samples were recorded on a homemade setup equipped with an Ar^+ ion laser (Spectra-Physics Stabilite 2017) as an excitation beam source, a spectrometer (Horiba Jobin Yvon TRIAX 550), and a charge-coupled device (CCD) detector (Horiba Jobin Yvon Symphony) cooled at −196 °C. The wavelength of the excitation beam was 514.5 nm. The diffuse-reflectance UV–vis spectra of the samples were recorded on a Varian Cary 5000 UV–vis–NIR spectrophotometer equipped with an integrating sphere. Dehydrated barium sulfate was used as the reference. Zero-field cooled (ZFC) susceptibility measurements of A-*n* samples were conducted from 4 to 300 K in a magnetic field of 1000 Oe on a superconducting quantum interference device (SQUID) magnetometer (MPMS5) at the Korea Basic Science Institute located at Korea University. Electron spin resonance (ESR) spectra were measured at room temperature on a Bruker EMX 300 electron spin resonance spectrometer at the Korea Basic Science Institute. The same amount of dehydrated sample (250 mg), same power, and same microwave frequency were used in all A-*n* and H-*n* samples to obtain the relative intensity. Powder X-ray diffraction (XRD) patterns were obtained on a Rigaku D/MAX-2500/pc diffractometer. The Brunauer–Emmett–Teller (BET) and Langmuir surface areas were obtained from argon adsorption isotherms at 87.3 K by use of a Quantachrome Autosorb-1. The samples were evacuated under a vacuum (3×10^{-7} Torr) at 160 °C prior to analysis.

RESULTS AND DISCUSSION

Size-Controlled Syntheses of Monodisperse AM-6 and VSH-1 Crystals. Syntheses of monodisperse AM-6 and VSH-1 crystals were achieved by optimization of the corresponding gel compositions. The size variation while retaining monodispersity was effectively achieved by varying the mole ratios of H_2SO_4 and KOH for AM-6 (from 0.2 to 3 μm) and VSH-1 crystals (from 0.3 to 10 μm). Thus, in the case of AM-6, the increase in the mole ratio of H_2SO_4 leads to the size increase (up to 3 μm). To produce larger AM-6 crystals with $L_{[110]}$ of 5 and 10 μm, respectively, the simultaneous decrease in the mole ratio of SiO_2 was necessary. In the case of VSH-1, the increase in the mole ratio of KOH leads to the size increase. The AM-6 crystals with $L_{[110]}$ of 0.2, 1, 3, 5, and 10 μm are denoted as A-0.2, A-1, A-3, A-5, and A-10, respectively. The VSH-1 crystals with $L_{[110]}$ of 0.3, 1, 3, 5, and 10 μm are denoted as H-0.3, H-1, H-3, H-5 and H-10, respectively. Collectively, they will be denoted as A-*n* and H-*n*.

The typical SEM images of A-*n* and H-*n* (Figure 2) show that they are indeed highly crystalline and uniform in size. A-0.2 and A-3 adopt a square bifrustum shape, A-1 adopts a brick shape, and A-5 and A-10 adopt a tile shape. H-*n* crystals generally adopt a pseudo-octahedral shape. However, the degree of truncation along the *c* axis is variable: none in the case of H-0.3 and H-3, small in the case of H-1 and H-5, and large in the case of H-10.

Quality of A-*n* and H-*n* Crystals. For this work, the quality of A-*n* samples is critical. X-ray powder diffraction patterns of the A-*n* and H-*n* samples (Figure 3) and their high surface areas (Table SI-2, Supporting Information) further confirmed their high crystallinities, regardless of their sizes. In the case of A-*n*, we measured high resolution Ar adsorption isotherms (Figure SI-2, Supporting Information). The micropore volumes (in cubic centimeters per gram) measured by the *t*-plot method ranged between 0.128 and 0.139, and those estimated by the value at $p/p_0 = 0.11$ ranged between 0.149 and 0.158. The total pore volumes at $p/p_0 = 0.99$ (in cubic centimeters per gram) ranged between 0.191 and 0.255. The BET surface areas (in cubic meters per gram) ranged between 415 and 435. However, we could not obtain theoretical pore volumes and surface areas of A-*n* samples because AM-6 has

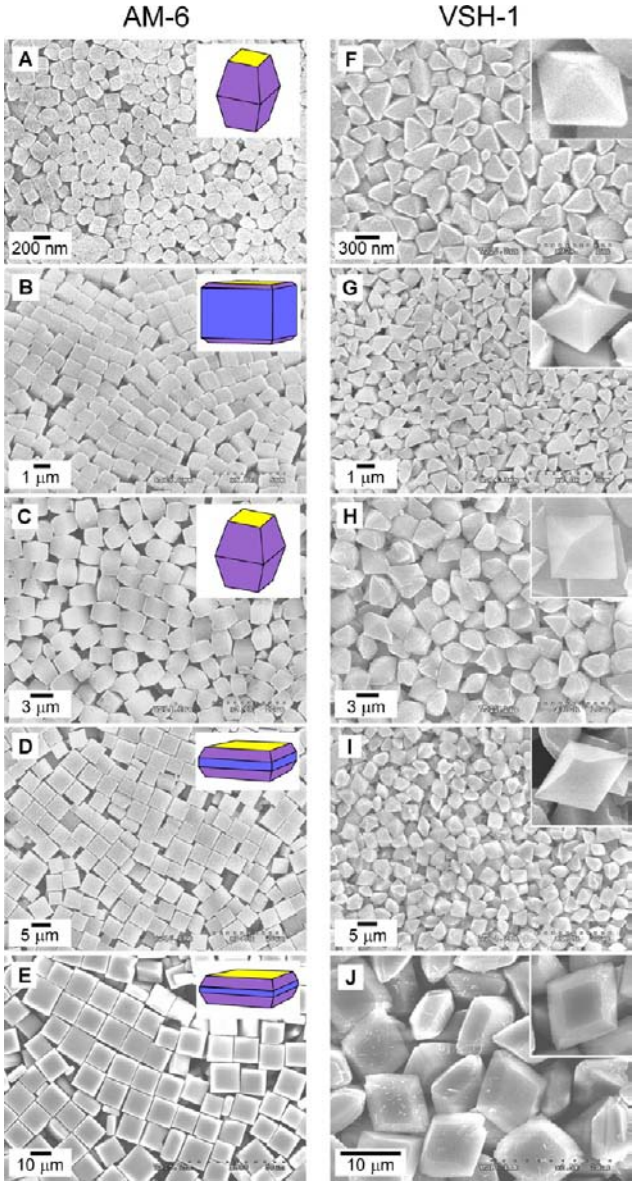

Figure 2. SEM images of (A) A-0.2, (B) A-1, (C) A-3, (D) A-5, (E) A-10, (F) H-0.3, (G) H-1, (H) H-3, (I) H-5, and (J) H-10. The inset in each panel for A-*n* illustrates the typical morphology for its size, and the inset in each panel for H-*n* shows a higher magnification SEM image.

large amounts of defects arising from the presence of at least two polymorphs within each crystal. Nevertheless, the SEM images, X-ray powder diffraction patterns, narrow pore size distributions, and high surface areas demonstrate that the quality of A-*n* and H-*n* samples is very high and they have no amorphous phases.

Effect of Length on Vibration Spectra. The full-range (200−1200 cm^{-1}) Raman spectra of A-*n* and H-*n* (Figure 4A,B) show that VO_3^{2-} quantum wires and the $(O{=}V^{IV}O_4)^{2-}$ quantum dots are well-preserved. Careful analysis of the vibrational bands of the VO_3^{2-} quantum wires along the wire direction (longitudinal vibration) revealed that ν progressively red-shifted (from 867.6 to 866.8, 866.2, 865.5, and 864.9 cm^{-1}) with increasing $L_{[110]}$ (Figure 4C). Such a phenomenon has not been observed for TiO_3^{2-} quantum wire[14] and also not for $(O{=}V^{IV}O_4)^{2-}$ quantum dots of H-*n* (Figure 4D). Because the

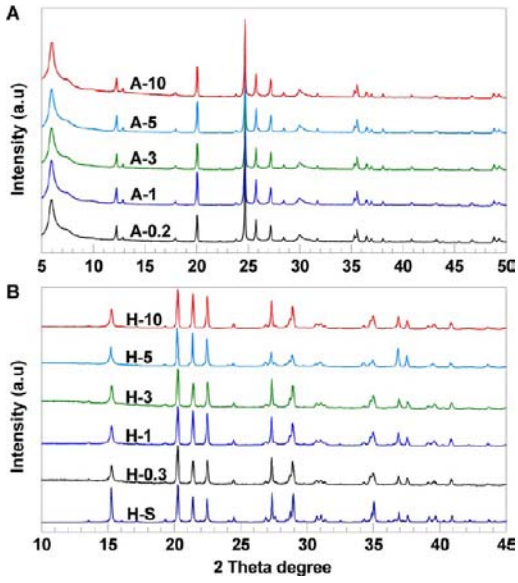

Figure 3. X-ray powder diffraction patterns of (A) A-*n* and (B) H-*n*. H-S in panel B represents the simulated diffraction pattern.

most important difference between VO_3^{2-} and TiO_3^{2-} wires is that the former has an unpaired d^1 electron on each V^{IV} while the latter has not (d^0), we conclude that the above interesting phenomenon arises from the increased degree of bond weakening of the VO_3^{2-} quantum wire along the wire direction, presumably due to the increased degree of repulsive spin−spin interaction between the neighboring V^{IV} centers as *l* increases (vide infra).

Furthermore, despite the fact that the total number of VO_3^{2-} quantum wires existing in a given amount of sample (1 g) decreased from 9.7×10^{18} (for A-0.2) to 2.3×10^{18} (for A-10) with increasing $L_{[110]}$ (due to the increase in *l*; see Supporting Information for the calculation procedure), the intensity of the longitudinal vibrational band progressively increased with increasing $L_{[110]}$, indicating that the susceptibility of the longitudinal vibration to the laser beam increases with increasing *l* (Figure 4E). However, the bandwidth (full width at half-maximum, fwhm) remained very narrow (9.5−10 cm^{-1}) and nearly constant, showing that the length homogeneity of the wires in each A-*n* sample is high. A similar phenomenon was observed for the TiO_3^{2-} quantum wire.[14] In the case of H-*n*, however, the Raman spectra remained the same regardless of the crystal size (Figure 4D).

In the case of TiO_3^{2-} quantum wire, the bending (transverse) vibration appears in the 274−280 nm region.[10] In the case of A-*n*, however, two bands that appear between 259 and 270 nm and between 310 and 340 nm shift to the lower-energy region with increasing length of the $V^{IV}O_3^{2-}$ quantum wire (266.0, 265.1, 264.6, 263.9, and 263.4nm and 328.8, 328.2, 327.8, 327.0, and 326.5 nm for n = 0.2, 1, 3, 5, and 10, respectively.) We assign these two bands as the bending vibrational bands. The vibrational intensities increased (although slightly) as the length of the $V^{IV}O_3^{2-}$ quantum increased. Thus, both stretching and bending vibrations of $V^{IV}O_3^{2-}$ wire shift to lower energy regions and their intensities increase as the length of the quantum wire increases.

Effect of Length on ESR Spectra. In the case of electron spin resonance (ESR) spectra of A-*n* (Figure 5A), despite the fact that the numbers of V^{IV} centers is the same (because the loaded amounts of A-*n* in the ESR cell are the same), the

dx.doi.org/10.1021/ja307187z | J. Am. Chem. Soc. 2012, 134, 17202−17211

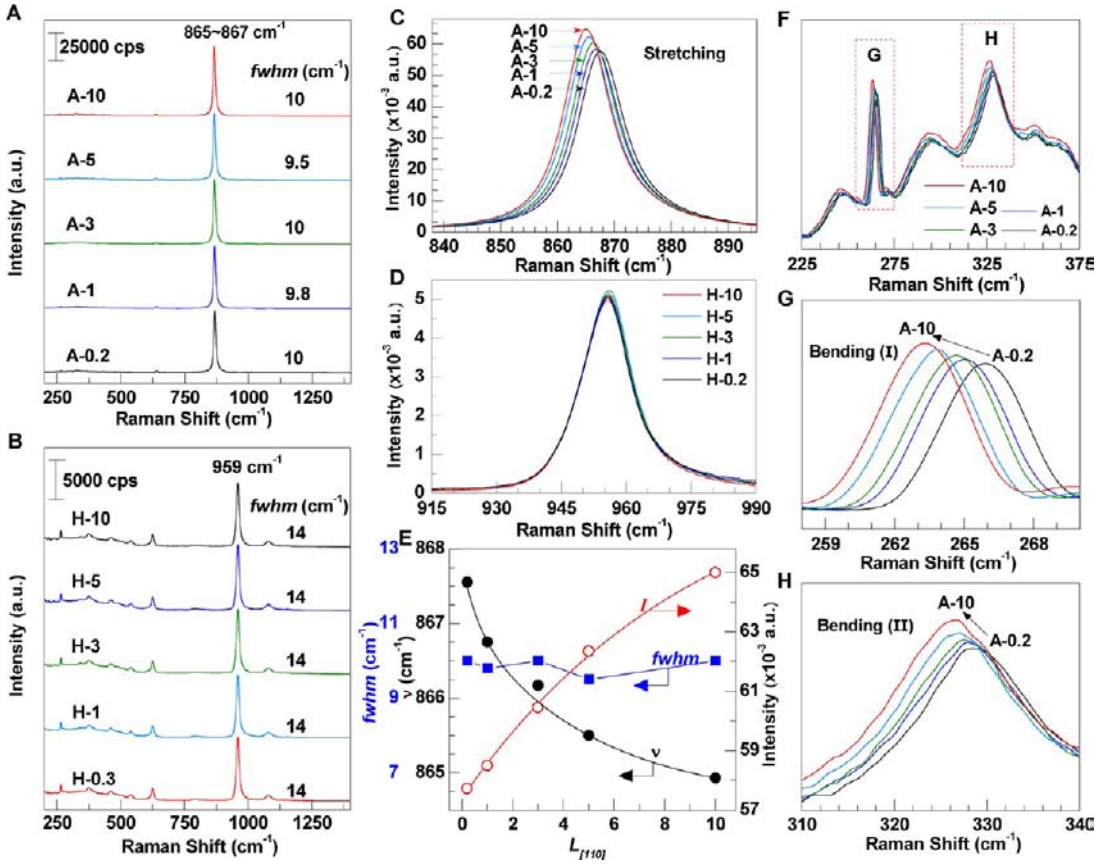

Figure 4. (A, B) Raman spectra of dehydrated (A) A-*n* and (B) H-*n* in the 200−1400 cm^{-1} region. (C, D) Raman spectra of (C) longitudinal stretching vibration of VO_3^{2-} quantum wires in A-*n* and (D) O═V stretching of the $(O═VO_4)^{2-}$ quantum dots in H-*n*. (E) Plots of intensity (*I*), frequency (ν), and peak width (fwhm) of the longitudinal vibration of VO_3^{2-} quantum wires in A-*n* with respect to $L_{[110]}$. (F) Raman spectra of dehydrated A-*n* in the 225−375 cm^{-1} region. (G, H) Raman spectra of transverse bending vibration of VO_3^{2-} quantum wires in A-*n* in (G) 258−270 and (H) 310−340 cm^{-1} regions.

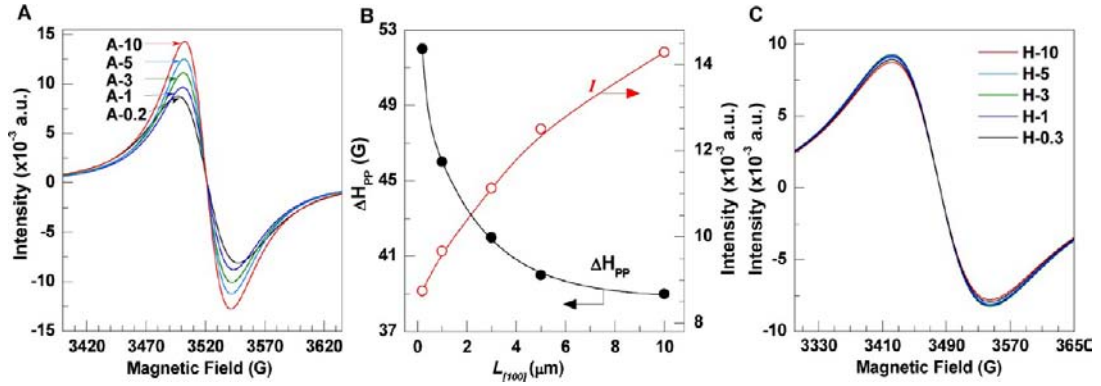

Figure 5. (A) ESR spectra of A-*n*. (B) Plots of ESR intensity and ΔH_{pp} of A-*n* with respect to $L_{[110]}$. (C) ESR spectra of H-*n* at room temperature.

intensity increased with increasing *I* while the peak-to-peak width (ΔH_{pp}) decreased (Figure 5A,B). The signal broadens and finally become immeasurable if relaxation time decreases or relaxation occurs rapidly. On this basis, the sharpening of the ESR signal indicates that the overall relaxation time increases as the length of the VO_3^{2-} quantum wire increases.[25]

In fact, there are two types of relaxation, spin−lattice and spin−spin. Spin−lattice relaxation relates to the characteristic lifetime of the spin state and is determined by the dissipation of spin energy via thermal vibration of the lattice. Spin−spin relaxation involves energy transfer between interacting spins via dipole and exchange interactions. Usually, spin−spin relaxation time is much shorter than spin−lattice relaxation time and thus is the dominant contributing factor to the ESR line width (ΔH_{pp}).

As demonstrated in the previous section, the intensities of both longitudinal stretching vibration and transverse bending vibration increase with increasing $L_{[110]}$. Accordingly, it is expected that the spin−lattice relaxation time will decrease with increasing length of the $V^{IV}O_3^{2-}$ wire, leading to broadening of the ESR signal (increase of ΔH_{pp}). However, the result is opposite. This leads to an interesting conclusion that the spin−

dx.doi.org/10.1021/ja307187z | J. Am. Chem. Soc. 2012, 134, 17202−17211

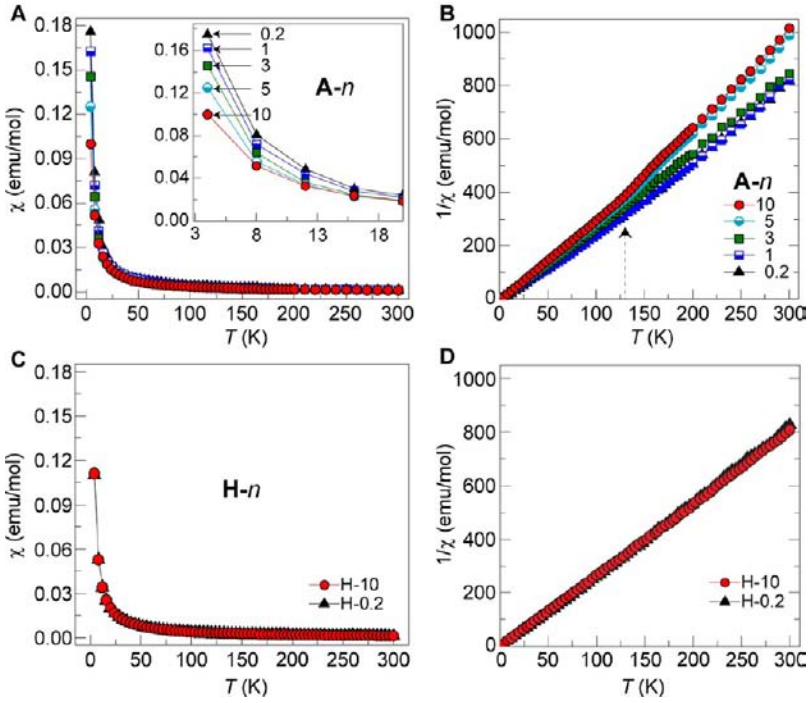

Figure 6. Plots of (A, C) magnetic susceptibility (χ) and (B, D) reciprocal magnetic susceptibility ($1/\chi$), with respect to T, for A-n and H-n as indicated.

spin relaxation time, the more dominant factor to ΔH_{pp}, increases with increasing length of the $V^{IV}O_3^{2-}$ wire. This means that the degree of spin energy transfer between the neighboring d^1 spins decreases as they are interlinked by the bridging oxygen. The repulsive spin−spin interaction proposed in the previous section may be responsible for the increase in the spin−spin relaxation time.

In the case of H-n, however, the ESR spectra remained the same regardless of the crystal size (Figure 5C). This result indicates that the d^1 electron residing on oxovanadate $(O{=}V^{IV}O_4)^{2-}$ does not interact with those in the neighbor because the $V^{IV}-V^{IV}$ distance in H-n is much larger (6.0−8.29 Å) than that in VO_3^{2-} quantum wire (3.717 Å) (Figure 1).

Effect of Length on Magnetic Susceptibility. The magnetic susceptibility (χ) data of A-n samples (Figure 6A) revealed that VO_3^{2-} quantum wire is ferromagnetic, consistent with the report of Howe and co-workers.[26] The measured atomic magnetic moment values were 1.80, 179, 1.76, 1.72, and 1.71 times μ_B for A-0.2, -1, -3, -5, and -10, respectively, at $T <$ 125 K. This indicates that the oxidation state of most of the V ions in A-n is +4. Consistent with this, while the theoretical M/V atomic ratio should be 2 (M = Na or K or combined) for an ideal A-n, the M/V ratios observed from A-n samples were 1.99, 1.99, 1.97, 2.01, and 1.98, respectively, indicating that the oxidation states of almost all of the V ions in A-n are +4. In the case of H-n, the measured atomic magnetic moment values were 1.71 μ_B and 1.73 μ_B for H-0.2 and H-10, respectively. While the theoretical M/V atomic ratio should be 2 (M = Na or K or combined) for an ideal H-n, the M/V ratios observed from H-0.2 and H-10 were 1.97 and 1.99, respectively. The above results also demonstrate that the oxidation states of almost all V ions in H-n are +4.

In the case of A-n, χ progressively decreased with increasing l in the temperature (T) region between 4 and 20 K, indicating that the degree of magnetic field-induced spin ordering decreases with increasing l at lower temperatures (Figure 6A, inset). Such a phenomenon is more pronounced at $T >$ 125 K (Figure 6B). Thus, while the measured atomic magnetic moment values were between 1.71μ_B and 1.8μ_B at $T <$ 125 K, the corresponding values were 1.66, 1.66, 1.65, 1.56, and 1.54 times μ_B at $T >$ 125 K for n = 0.2, 1, 3, 5, and 10, respectively. This result indicates that the degree of spin ordering decreases with increasing l, in particular at $T >$ 125 K. H-n is also ferromagnetic (Figure 6C). However, the χ values of H-n at $T <$ 20 K remained the same regardless of $L_{[110]}$ and the relationship between $1/\chi$ and T remained linear in the whole region of T (Figure 6D), supporting that the variation of χ in the case of the VO_3^{2-} quantum wire indeed arises from the variation of l.

Effect of Length on Band Gap Energy. The diffuse reflectance UV−vis spectra of A-n, H-n (both dehydrated, 90% Na^+ and 10% K^+ and 1 g each), and Na_2VO_3 (1 g) showed the presence of V^{IV} d−d transition bands in the lower energy (0.7−3.5 eV) region and $V^{IV} \rightarrow O$ charge-transfer (CT) bands[22] in the higher energy (3.5−6.2 eV) region (Figure 7A). The spectrum of Na_2VO_3 in Figure 7A represents a spectrum of three-dimensional vanadate. As noted, in all three cases, the $V^{IV} \rightarrow O$ CT bands are much stronger in intensity than V^{IV} d−d transition bands, showing that the d−d transitions are also Laporte (parity) forbidden, which is a general phenomenon for a d−d transition.

The d−d transition bands of the VO_3^{2-} quantum wire (denoted as B_1, B_2, and B_3) appear at 1.11, 2.11, and 3.12 eV, respectively, and those of $[O{=}VO_4]^{2-}$ (denoted as C_1, C_2, and C_3) appear at 1.41, 2.10, and 2.78 eV, respectively (Figure 7B). However, those of Na_2VO_3 are not well resolved. In fact, it has been proposed that each V^{IV} ion in the $V^{IV}O_3^{2-}$ quantum wire exists in a distorted (flattened) octahedral environment:

$$-O_{ax}-[V^{IV}(O_{eq})_4]-O_{ax}-[V^{IV}(O_{eq})_4]-O_{ax}-$$

dx.doi.org/10.1021/ja307187z | J. Am. Chem. Soc. 2012, 134, 17202−17211

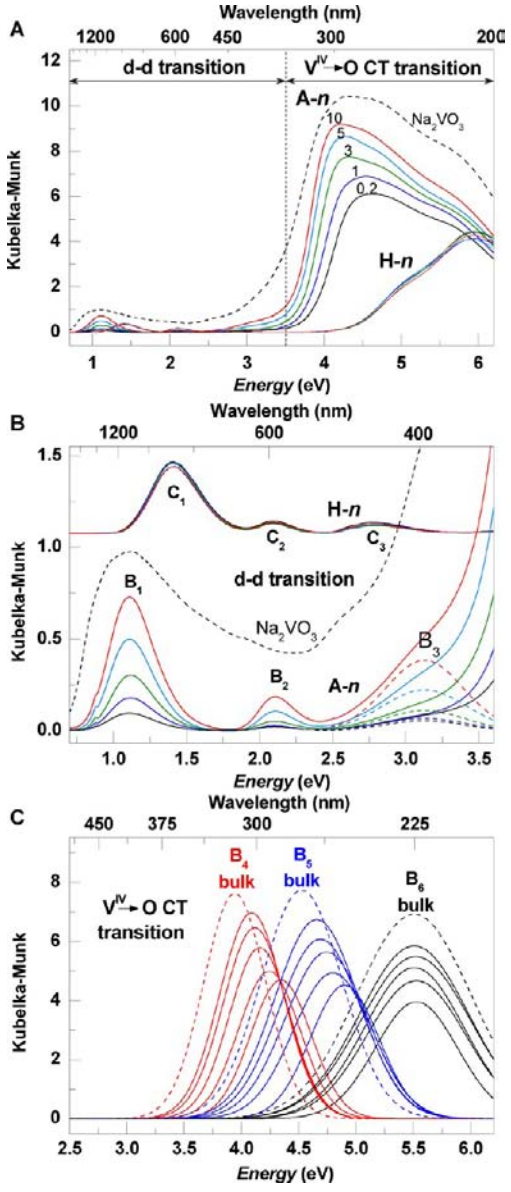

Figure 7. (A) Diffuse-reflectance UV−vis spectra of A-*n*, H-*n*, and Na_2VO_3 as indicated. (B) Diffuse-reflectance UV−vis spectra of A-*n*, H-*n*, and Na_2VO_3 (as indicated) in the d−d transition region. (C) Deconvoluted diffuse reflectance spectra of A-*n* and Na_2VO_3 (as indicated) in the $V^{IV} \rightarrow O$ CT band region.

where O_{ax} denotes the axial O atom, which interlinks two neighboring V^{IV} ions, and O_{eq} denotes the equatorial O atom, which links the V^{IV} ion to Si, with the distance between V^{IV} and O_{ax} being shorter than that between V^{IV} and O_{eq}.[9] In this symmetry the two degenerate t_{2g} and e_g orbitals split into [d_{xy} and (d_{xz}, d_{yz})] and [$d_{x^2-y^2}$ and d_{z^2}], respectively (Figure SI-5, Supporting Information).[18] Accordingly, we attribute the three d−d transition bands to $d_{xy} \rightarrow (d_{xz}, d_{yz})$, $d_{xy} \rightarrow d_{x^2-y^2}$, and $d_{xy} \rightarrow d_{z^2}$ transitions, respectively.

The $V^{IV} \rightarrow O$ CT bands of A-*n* and Na_2VO_3 were best deconvoluted into three bands, denoted as B_4, B_5, and B_6, respectively (Figure 7C), while the corresponding $V^{IV} \rightarrow O$ CT bands of H-*n* were best deconvoluted into two bands, denoted as C_4 and C_5, respectively (Supporting Information). Interestingly, while the absorption intensities of VO_3^{2-} quantum wires (A-*n*) progressively increased with increasing $L_{[110]}$, those of $(O{=}VO_4)^{2-}$ (H-*n*) remained constant (Figure 7A,B). Furthermore, in the case of A-*n*, two low-energy CT bands (B_4 and B_5) progressively red-shifted with increasing $L_{[110]}$ (Figure 7C, B_4 = 4.35, 4.24, 4.16, 4.10, and 4.08 eV and B_5 = 4.91, 4.81, 4.74, 4.68, and 4.66 eV, respectively), while the highest-energy CT band (B_6) remained constant at 5.51 eV. Nevertheless, the intensity of B_6 progressively increased with increasing $L_{[110]}$.

It is now clear that the interesting *l*-dependent changes of optical properties of $V^{IV}O_3^{2-}$ quantum wires (increases in the absorptions of B_1−B_6 and red shifts of the B_4 and B_5 CT bands) do not arise due to the scattering effect caused by the crystal size increase (as demonstrated by the behavior of H-*n*) but arise due to the increase in *l*.

The E_g values of VO_3^{2-} quantum wires were deduced from B_4 bands, which were 4.35, 4.24, 4.16, 4.10, and 4.08 eV. The differences between E_g of the bulk vanadate (Na_2VO_3, 3.94 eV) and those of A-*n* (denoted as ΔE_g) are 0.41, 0.30, 0.22, 0.16, and 0.14 eV. Because the effective mass approximation has been shown to be quite useful for analysis of the l−E_g relationship of semiconductor nanorods,[4,5,13,27−30] the obtained ΔE_g values were forced to fit into eq 2:

$$\Delta E_g = \frac{h^2}{4\mu_{xy}d^2} + \frac{h^2}{8\mu_z l^2} \quad (2)$$

For the above, we estimated the minimum average *l* of VO_3^{2-} quantum wire in A-0.2 to be 50 nm from analysis of the TEM images (Figure 8). In fact, AM-6 is inherently an intergrowth structure, consisting of randomly stacked polymorph A, B, and other minor polymorph layers. As a result, AM-6, like ETS-10, is expected to have many defects, leading to disconnection of

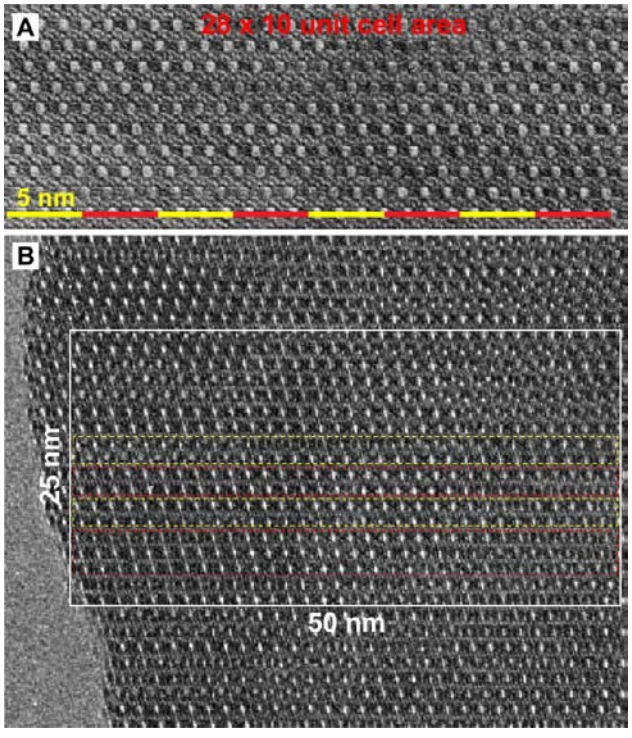

Figure 8. High-resolution electron microscopy images of A-0.2 showing (A) the region where 28 × 10 unit cells are stacked regularly without having stacking faults and (B) the region where more than 50 nm length regions are free from stacking faults.

dx.doi.org/10.1021/ja307187z | J. Am. Chem. Soc. 2012, 134, 17202−17211

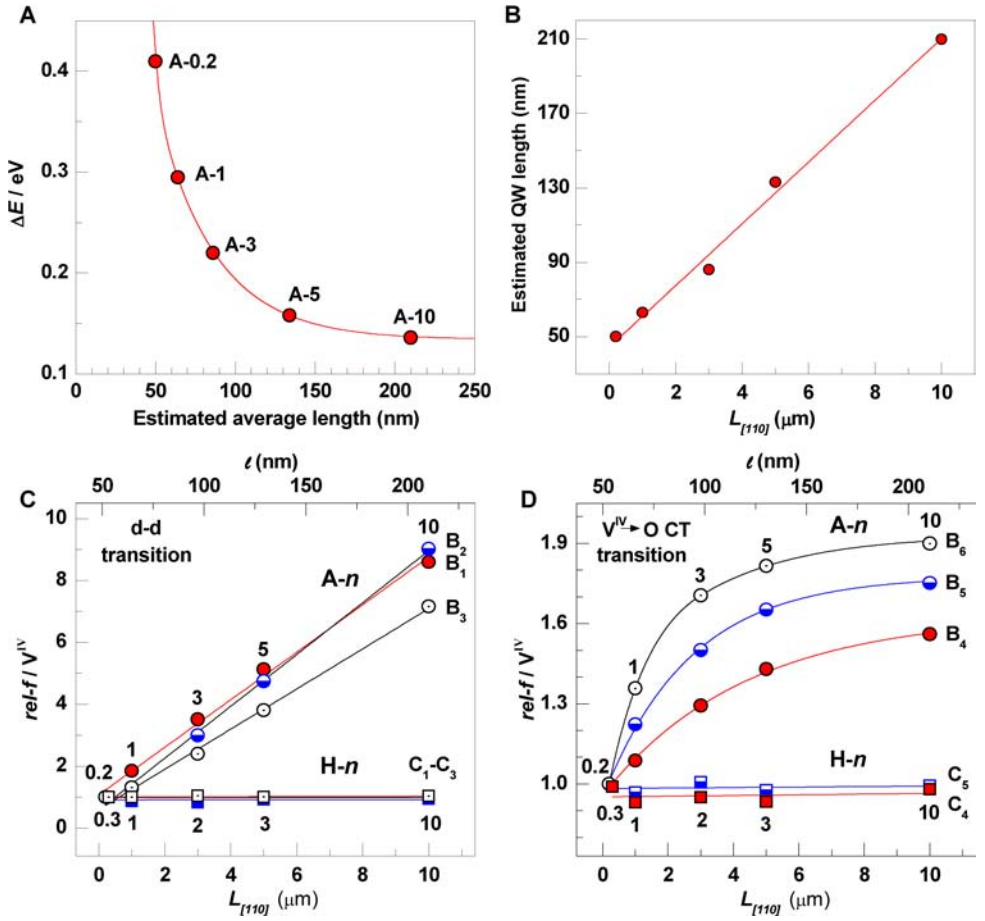

Figure 9. (A) Forced fitting of ΔE_g values between the E_g values of VO_3^{2-} quantum wires and that of Na_2VO_3 based on the effective mass approximation theory (eq 2 in the text) to obtain the estimated lengths of VO_3^{2-} quantum wires. (B) Linear relationship between quantum wire and crystal size ($L_{[110]}$). (C) Plots of rel-*f* for the d−d transition per V^{4+} ion (rel-*f*/V^{IV}) for A-*n* and H-*n* with respect to $L_{[110]}$. (D) Plots of rel-*f* for the CT transition per V^{4+} ion (rel-*f*/V^{IV}) for A-*n* and H-*n* with respect to $L_{[110]}$.

VO_3^{2-} quantum wires. However, from the A-*n* series, we have found that there are many regions like the high-resolution TEM image shown in Figure 8A in the case of A-0.2, where no stacking fault exists within the 28 × 10 unit cell area. Furthermore, we have found many 50 nm length regions from A-0.2 where no stacking faults appear; a typical image is shown in Figure 8B. This observation allows us to conclude that the average lengths of long VO_3^{2-} quantum wires are longer than 50 nm in A-0.2, whose spectra determine the absorption onsets of B_4 V^{IV} → O CT band and E_g values. On this basis, we set 50 nm as the average length that determines E_g.

The result of fitting the ΔE_g values to the effective mass approximation theory with 50 nm as the initial length is shown in Figure 9A. This fit allows us to extract the estimated average *l* values from A-*n*, which are 50, ∼63, ∼85, ∼134, and ∼210 nm. Interestingly, a linear relationship was found between $L_{[110]}$ and *l* (Figure 9B). This result shows that the quantum confinement effect still shows up in VO_3^{2-} quantum wires with lengths of ∼210 nm. This also indicates the remarkable fact that the Bohr length is longer than ∼200 nm. The above fit (Figure 9A) also elucidates the μ_{xy} and μ_z values, which are $15.7m_e$ and $0.0005m_e$, respectively. These values are very similar to those of TiO_3^{2-} wire ($\mu_{xy} = 15.2m_e$ and $\mu_z = 0.0006m_e$), indicating that in the case of the VO_3^{2-} quantum wire the transverse electron mobility is very low while the longitudinal electron mobility is very high despite its oxide nature.

Effect of Length on Oscillator Strength. Many scientists have proposed that per-unit-cell oscillator strength (per-unit-cell *f*) will increase as the size of the quantum dot decreases within the Bohr radius region. Thus, the research groups of Brus,[15] Takagahara,[31] Kayanuma,[32] Hanamura,[33] Wang et al.,[34] Itoh et al.,[35] Nozik and co-workers,[36] Yoffe,[37] Weller and co-workers,[38] Schmelz et al.,[39] and Alivisatos and co-workers[40] have theoretically proposed or experimentally demonstrated that per-unit-cell *f* is proportional to $1/r^3$ (*r* is radius) and per-particle *f* remains constant with respect to *r* in the strong and medium confinement regions. On the other hand, the research groups of Klimov,[41] Bawendi,[42] Peng,[43] and Ozin[44] showed that per-unit-cell *f* and per-particle *f* vary differently with varying sizes of quantum dot. In particular, Ozin and co-workers[44] demonstrated that per-particle *f* of PbS nanoparticles increases with respect to $r^{3.2}$, as if their sizes belong to the weak confinement region, despite the fact that their sizes are much smaller than a_B of PbS (16 nm).[45] Our group also demonstrated that, in the case of titanate quantum sheets, per-unit-cell *f* increases with increasing area of the quantum sheets.[46] Thus, there is no consistent relationship between the size of quantum dots or quantum sheets and the per-unit cell *f*. In that sense, it is of great interest to elucidate the relationship

dx.doi.org/10.1021/ja307187z | J. Am. Chem. Soc. 2012, 134, 17202−17211

between the length of VO_3^{2-} wire and per-unit-cell *f* or per-V^{IV}-ion *f*.

In general, for a light-absorbing molecule, the oscillator strength (*f*) is usually obtained from eq 3:[38,47]

$$f = 4.32 \times 10^{-9} \int_{\nu_1}^{\nu_2} \varepsilon \, d\nu \quad (3)$$

where ε and ν represent the extinction coefficient (in $cm^{-1}\cdot M^{-1}$) of the light absorbing molecule and wavenumber (in cm^{-1}), respectively. However, because A-*n* and H-*n* are insoluble particles, their absolute *f* values could not be obtained. Instead, with the bands of A-0.2 and H-0.3 as self-references, relative per-V^{IV}-ion oscillator strength (rel-*f*/V^{IV}) values of B_1−B_6 and C_1−C_5 were obtained by dividing their Kubelka−Munk areas by the corresponding area of A-0.2 and H-0.3, respectively.

The plots of rel-*f* values for B_1−B_3 and C_1−C_3 per-V^{4+}-ion (rel-*f*/V^{IV}) with respect to $L_{[110]}$ (Figure 9C) show that rel-*f*/V^{IV} values of B_1−B_3 linearly increase with increasing *l* from 50 to 210 nm (by ∼4 times), reaching 7−9 times increases, while those of C_1−C_3 remain constant at 1. This is the first case to show the increase in *f* for the d−d transition with increasing *l* of the quantum wire. The rel-*f*/V^{IV} values of B_4−B_6 CT bands also increased, although nonlinearly, reaching 1.5−1.9 times increase in the case of A-10. However, those of C_4 and C_5 also remained constant at 1 (Figure 9C,D). This result shows that the per-ion *f* values for the absorption bands of quantum wires increase with increasing lengths within Bohr length regions. This phenomenon is likened to the result of TiO_3^{2-} quantum sheets[46] and PbS quantum dots.[44]

In fact, the oscillator strength for a d−d transition is intrinsically small because it is parity-forbidden (transition from a gerade symmetry to another gerade symmetry). In such a case the vibration of the complex leads to the increase in oscillator strengths owing to the symmetry perturbation or by the action of odd parity vibrations.[48]Accordingly, we attribute the above length-dependent increase in rel-*f*/V^{IV} value for the d−d transition to the increase in the degree (intensity) of vibration of the VO_3^{2-} quantum wire, as demonstrated in Figure 4. We also attribute the length-dependent increase in rel-*f*/V^{IV} value for the V^{IV} → O CT transition to the increase in the degree of vibration of the VO_3^{2-} quantum wire. Because the CT transition is parity-allowed in the case of an octahedral system, we expect that the degree of vibration-induced increase in rel-*f*/V^{IV} will be less for the CT transition than for the d−d transition, and this may be the reason why the degree of *rel-f*/V^{IV} value increase is much higher for the d−d transition (7−9 times) than for the CT transition (1.5−1.9 times).

CONCLUSION

We have developed for the first time the methods to synthesize pure, highly crystalline, monodisperse, and all-V^{IV} AM-6 and VSH-1 crystals with sizes ($L_{[110]}$) ranging between 0.2−0.3 and 10 μm. AM-6 contains VO_3^{2-} quantum wires, and VSH-1 contains isolated oxovanadate $[O{=}VO_4]^{2-}$ quantum dots. In the case of AM-6, *l* of the VO_3^{2-} quantum wire linearly increases as $L_{[110]}$ increases. In the case of VSH-1, the number of $[O{=}VO_4]^{2-}$ merely increases as $L_{[110]}$ increases. Both the VO_3^{2-} quantum wire and $[O{=}VO_4]^{2-}$ quantum dot show multiple V^{IV} d−d transitions in the 0.7−3.5 eV region and V^{IV} → O CT transitions in the 3.5−6.2 eV region. In the case of the VO_3^{2-} quantum wire, per-V^{IV}-ion oscillator strength of the d−d transition increases by 7−9 times and that of CT transition increases by 1.5−1.9 times with increasing *l* from ∼50 to 210 nm (by ∼4 times). In the case of $[O{=}VO_4]^{2-}$ quantum dots, however, per-V^{IV}-ion oscillator strengths remain constant for both d−d and CT transitions regardless of the crystal size. The band gap energy (E_g) of the VO_3^{2-} quantum wire progressively decreases with increasing *l* even when it reaches ∼210 nm, indicating that the Bohr length is longer than 200 nm. The deduced μ_z and μ_{xy} are $0.0005m_e$ and $15.7m_e$, respectively, predicting that the longitudinal exciton mobility is very high. The longitudinal vibration frequency ν of the VO_3^{2-} quantum wire decreases and the intensity of the vibration band increases as *l* increases. The ESR intensity also increases while the peak-to-peak width decreases as *l* increases, indicating that the spin−spin relaxation rate R_{ssr} decreases as *l* increases. The magnetic susceptibility χ decreases as *l* increases, especially at $T > 125$ K, indicating that the tendency of the d^1 electron spins to orient to the external magnetic field decreases with increasing *l*. The per-V^{IV}-ion oscillator strengths for both d−d and CT transitions (*f*), ESR intensities, ESR peak width (ΔH_{pp}), longitudinal vibrational frequency (ν), and magnetic susceptibility (χ) seem to be tightly coupled.

ASSOCIATED CONTENT

Supporting Information

Additional text, five figures, and two tables showing X-ray powder diffraction pattern of Na_2VO_3, Ar adsorption isotherms of A-*n*, estimated numbers of quantum wires, relative Raman intensities, and deconvolution of the V^{IV} → O CT band for A-*n*. This material is available free of charge via the Internet at http://pubs.acs.org.

AUTHOR INFORMATION

Corresponding Author

yoonkb@sogang.ac.kr

Notes

The authors declare no competing financial interest.

ACKNOWLEDGMENTS

We thank the Korea Center for Artificial Photosynthesis (KCAP), located in Sogang University and funded by MEST through the National Research Foundation of Korea (NRF-2011-C1AAA001-2011-0030278), and the acceleration program of the NRFK (2012R1A2A3A01009806). We thank Jiyun Lee for providing us Figure 1. We also thank Yong Min Lee for the ESR measurements.

REFERENCES

(1) (a) Venkataraman, L.; Lieber, C. M. *Phys. Rev. Lett.* **1999**, *83*, 5334−5337. (b) Ouyang, M.; Huang, J.-L.; Lieber, C. M. *Acc. Chem. Res.* **2002**, *35*, 1018−1025.

(2) (a) Golden, J. H.; DiSalvo, F. J.; Frechet, J. M. J.; Silcox, J.; Thomas, M.; Elman, J. *Science* **1996**, *273*, 782−784. (b) Xia, Y.; Yang, P.; Sun, Y.; Wu, Y.; Mayers, B.; Gates, B.; Yin, Y.; Kim, F.; Yan, H. *Adv. Mater.* **2003**, *15*, 353−389.

(3) (a) Ahrenkiel, S. P.; Miedaner, O. I.; Curtis, C. J.; Nedeljković, J. M.; Nozic, A. J. *Nano Lett.* **2003**, *3*, 833−837. (b) Yu, H.; Li, J.; Loomis, R. A.; Wang, L.-W.; Buhro, W. E. *Nat. Mater.* **2003**, *2*, 517−520. (c) Duan, X.; Huang, Y.; Cui, Y.; Wang, J.; Lieber, C. M. *Nature* **2001**, *409*, 66−69.

(4) (a) Li, L.-S.; Hu, J.; Yang, W.; Alivisatos, A. P. *Nano Lett.* **2001**, *1*, 349−351. (b) Golden, J. H.; Deng, H.; DiSalvo, F. J.; Frechet, J. M. J.; Thompson, P. M. *Science* **1995**, *268*, 1463−1466.

(5) Kan, S.; Mokari, T.; Rothenberg, E.; Banin, U. *Nat. Mater.* **2003**, *2*, 155−158.

(6) Huang, Y.; Duan, X.; Cui, Y.; Lauhon, L. J.; Kim, K.-H.; Lieber, C. M. *Science* **2001**, *294*, 1313−1316.
(7) Bachtold, A.; Hadley, P.; Nakanishi, T.; Dekker, C. *Science* **2001**, *294*, 1317−1320.
(8) (a) Kuznicki, S. M. U.S. Patent 4853202, 1989. (b) Anderson, M. W.; Terasaki, O.; Ohsuna, T.; Philippou, A.; MacKay, S. P.; Ferreira, A.; Rocha, J.; Lidin, S. *Nature* **1994**, *367*, 347−351.
(9) (a) Anderson, M. W.; Terasaki, O.; Ohsuna, T.; Malley, P. J. O.; Philippou, A.; MacKay, S. P.; Ferreira, A.; Rocha, J.; Lidin, S. *Philos. Mag. B* **1995**, *71*, 813−841. (b) Wang, X.; Jacobson, A. J. *Chem. Commun.* **1999**, 973−974.
(10) Jeong, N. C.; Lee, Y. J.; Park, J.-H.; Lim, H.; Shin, C.-H.; Cheong, H.; Yoon, K. B. *J. Am. Chem. Soc.* **2009**, *131*, 13080−13092.
(11) (a) Yilmaz, B.; Warzywoda, J.; Sacco, A., Jr. *Nanotechnology* **2006**, *17*, 4092−4099. (b) Bordiga, S.; Palomino, G. T.; Zecchina, A.; Ranghino, G.; Giamello, E.; Lamberti, C. *J. Chem. Phys.* **2000**, *112*, 3859−3867.
(12) Jeong, N. C.; Lim, H.; Cheong, H.; Yoon, K. B. *Angew. Chem., Int. Ed.* **2011**, *50*, 8697−8701.
(13) Borello, E.; Lamberti, C.; Bordiga, S.; Zecchina, A.; Arean, C. O. *Appl. Phys. Lett.* **1997**, *71*, 2319−2321.
(14) Jeong, N. C.; Lee, M. H.; Yoon, K. B. *Angew. Chem., Int. Ed.* **2007**, *46*, 5868−5872.
(15) Brus, L. E. *J. Chem. Phys.* **1984**, *80*, 4403−4409.
(16) Pedersen, T. G. *Phys. Rev. B* **2003**, *67*, No. 073401.
(17) Rocha, J.; Brandao, P.; Lin, Z.; Anderson, M. W.; Alfredsson, V.; Terasaki, O. *Angew. Chem., Int. Ed.* **1997**, *36*, 100−102.
(18) (a) Shough, A. M.; Lobo, R. F.; Doren, D. J. *Phys. Chem. Chem. Phys.* **2007**, *9*, 5096−5104. (b) Shough, A. M.; Doren, D. J. *Chem. Mater.* **2009**, *21*, 1232−1241.
(19) Nash, M. J.; Rykov, S.; Lobo, R. F.; Doren, D. J.; Wachs, I. *J. Phys. Chem. C* **2007**, *111*, 7029−7037.
(20) Shough, A. M.; Doren, D. J.; Nash, M.; Lobo, R. F. *J. Phys. Chem. C* **2007**, *111*, 1776−1782.
(21) Ismail, M. N.; Fraiman, N. D.; Callahan, D. M., Jr.; Gursoy, G.; Viveiros, E.; Ozkanat, O.; Ji, J.; Willey, R. J.; Warzywoda, J.; Sacco, A., Jr. *Microporous Mesoporous Mater.* **2009**, *120*, 454−459.
(22) Datta, S. J.; Yoon, K. B. *Angew. Chem., Int. Ed.* **2010**, *49*, 4971−4975.
(23) Datta, S. J.; Yoon, K. B. *Microporous Mesoporous Mater.* **2011**, *143*, 115−124.
(24) Wang, X.; Liu, L.; Jacobson, A. J. *Angew. Chem.* **2001**, *113*, 2232−2234.
(25) Warren, D. C.; Fitzgerald, J. M. *Anal. Chem.* **1977**, *49*, 1840−1842.
(26) Yeates, R. M.; Murdoch, M. J.; Southon, P. D.; Mclaughlin, A. C.; Howe, R. F.; Bonino, F.; Bordiga, S.; Damin, A. *Dalton Trans.* **2009**, 8025−8032.
(27) Lamberti, C. *Microporous Mesoporous Mater.* **1999**, *30*, 155−163.
(28) Zimmerman, A. M.; Doren, D. J.; Lobo, R. F. *J. Phys. Chem. B* **2006**, *110*, 8959−8964.
(29) Steigerwald, M. L.; Brus, L. E. *Acc. Chem. Res.* **1990**, *23*, 183−188.
(30) Kayanuma, Y. *Phys. Rev. B* **1991**, *44*, 13085−13088.
(31) Takagahara, T. *Phys. Rev. B* **1987**, *36*, 9293−9296.
(32) Kayanuma, Y. *Phys. Rev. B* **1988**, *38*, 9797−9805.
(33) Hanamura, E. *Phys. Rev. B* **1988**, *37*, 1273−1279.
(34) (a) Wang, Y.; Suna, A.; McHugh, J.; Hilinski, E. F.; Lucas, P. A.; Johnson, R. D. *J. Chem. Phys.* **1990**, *92*, 6927−6939. (b) Wang, Y.; Herron, N. *J. Phys. Chem.* **1991**, *95*, 525−532.
(35) Itoh, T.; Furumiya, M.; Ikehara, T.; Gourdon, C. *Solid State Commun.* **1990**, *73*, 271−274.
(36) (a) Rajh, T.; Mićić, O. I.; Nozik, A. J. *J. Phys. Chem.* **1993**, *97*, 11999−12003. (b) Yu, P.; Beard, M. C.; Ellingson, R. J.; Ferrere, S.; Curtis, C.; Drexler, J.; Luiszer, F.; Nozik, A. J. *J. Phys. Chem. B* **2005**, *109*, 7084−7087.
(37) Yoffe, A. D. *Adv. Phys.* **1993**, *42*, 173−266.
(38) Vossmeyer, T.; Katsikas, L.; Giersig, M.; Popovic, I. G.; Diesner, K.; Chemseddine, A.; Eychmuller, A.; Weller, H. *J. Phys. Chem.* **1994**, *98*, 7665−7673.
(39) Schmelz, O.; Mews, A.; Basché, T.; Herrmann, A.; Müllen, K. *Langmuir* **2001**, *17*, 2861−2865.
(40) Striolo, A.; Ward, J.; Prausnitz, J. M.; Parak, W. J.; Zanchet, D.; Gerion, D.; Milliron, D.; Alivisatos, A. P. *J. Phys. Chem. B* **2002**, *106*, 5500−5505.
(41) Klimov, V. I. *J. Phys. Chem. B* **2000**, *104*, 6112−6123.
(42) Leatherdale, C. A.; Woo, W.-K.; Mikulec, F. V.; Bawendi, M. G. *J. Phys. Chem. B* **2002**, *106*, 7619−7622.
(43) Yu, W. W.; Qu, L.; Guo, W.; Peng, X. *Chem. Mater.* **2003**, *15*, 2854−2860.
(44) Cademartiri, L.; Montanari, E.; Calestani, G.; Migliori, A.; Guagliardi, A.; Ozin, G. A. *J. Am. Chem. Soc.* **2006**, *128*, 10337−10346.
(45) Wang, Y.; Herron, N.; Mahler, W.; Suna, A. *J. Opt. Soc. Am. B* **1989**, *6*, 808−813.
(46) Tae, E. L.; Lee, K. E.; Jeong, J. S.; Yoon, K. B. *J. Am. Chem. Soc.* **2008**, *130*, 6534−6543.
(47) Turro, N. J. *Modern Molecular Photochemistry*; Benjamin/Cummings: Menlo Park, CA, 1978; pp 86− 87.
(48) Kordas, J.; Avouris, P.; El-Bayoumi, M. A. *J. Phys. Chem.* **1975**, *79*, 2420−2423.